The Astronomical Journal, 125:2630–2644, 2003 May

FIRST OBSERVATIONS WITH A CO-PHASED SIX-STATION OPTICAL LONG-BASELINE ARRAY: APPLICATION TO THE TRIPLE STAR η VIRGINIS

C. A. Hummel,[1] J. A. Benson,[2] D. J. Hutter,[2] K. J. Johnston,[1] D. Mozurkewich,[3] J. T. Armstrong,[3] R. B. Hindsley,[3] G. C. Gilbreath,[3] L. J Rickard,[3] and N. M. White[4]

Received 2002 December 2; accepted 2003 January 28

ABSTRACT

We report on the first successful simultaneous combination of six independent optical telescopes in an interferometric array. This is double the number of independent telescopes, and 5 times the number of independent baselines, heretofore combined simultaneously. This was accomplished with the Navy Prototype Optical Interferometer at Lowell Observatory, near Flagstaff, Arizona. We describe the main technologies demonstrated, including hybrid six-way beam combination, nonredundant multiple optical path modulation for fringe separation, and the fringe detection electronics. To test the array's suitability for high-resolution stellar imaging, we observed the hierarchical triple star η Virginis, and we present the first images resolving all three components. The orbital motions of these stars were followed during winter and spring of 2002. Preliminary, astrometrically determined orbits of the two components in the close pair by reference to the tertiary were derived. This enabled the estimation of the mass ratio (1.27) of the components in the close pair. We also determined the relative orbital inclination to be 31°. Future work needed to improve the calibration of the data is discussed.

Key words: binaries: spectroscopic — binaries: visual — stars: fundamental parameters — stars: individual (η Virginis) — techniques: interferometric

1. INTRODUCTION

Earth-rotation interferometric aperture synthesis was pioneered in the radio spectrum and has achieved high sensitivity and imaging fidelity through the combination of as many as 27 (in the case of the Very Large Array) independent telescopes. The technique has been adopted by the optical interferometer community in order to obtain higher resolution. Even though the lack of coherent optical amplifiers would ultimately prevent the pairwise combination of this many optical telescopes, it is the complexity of a multitelescope array that has so far severely limited the number of telescopes in current arrays. Sacrificing the capability to image very complex sources in exchange for extreme resolution, they have been used for precise measurements of stellar diameters, limb darkening, and the separation of close double stars.

In this paper, we report the achievement of combining six telescopes simultaneously, a milestone in the pursuit of operating multitelescope arrays in the visible/near-infrared. This doubles the previously achieved number of telescopes combined simultaneously and quintuples the number of simultaneous baselines. The Navy Prototype Optical Interferometer (NPOI) at Lowell Observatory was designed for six-station operations and in September of 2001, after several years of three-station observations, was first used with a new beam combiner and control software to coherently combine six of its siderostats.

The NPOI and the project status as of 1998 were described in considerable detail by Armstrong et al. (1998). In the following, we will describe the hardware and software changes since 1998 that enabled the six-station operations. These include commissioning additional siderostats and delay lines, as well as installation of a new beam combiner, new fringe detection hardware, and a new control system. We will then present initial observations obtained with this array of the triple star η Virginis. We are able to present preliminary orbital solutions and to discuss the astrophysical parameters of this system. We conclude by commenting on some challenges related to stellar imaging with interferometers such as the NPOI.

2. INSTRUMENTATION UPDATES

2.1. *Commissioning of Imaging Siderostats*

The NPOI integrates an astrometric array and an imaging array. The four stations of the astrometric array (AE, AW, AN, and AC) are fixed and feature a laser metrology system for monitoring the siderostat pivot (Hutter & Elias 2002). Two additional transportable imaging siderostats have been placed on the East-2 (E2) and West-7 (W7) piers for the six-station commissioning observations. The baseline between AE and W7 is the longest at 64 m, while the shortest baseline is between E2 and AC, at 7.2 m. The unvignetted aperture is the same for all siderostats (35 cm) but is stopped down to 12 cm in diameter by the feed-system optics (beam compressors have not yet been installed). All stations are equipped with wave-front tip-tilt correctors. The light paths to the beam combination lab are evacuated.

The NPOI has six fast vacuum delay lines (FDLs) that can add up to 35 m of optical path each. These delay lines are used to track the atmospheric and sidereal motion of the

[1] US Naval Observatory, 3450 Massachusetts Avenue, NW, Washington, DC 20392-5420; cah@usno.navy.mil, kjj@usno.navy.mil.
[2] Navy Prototype Optical Interferometer, US Naval Observatory, Flagstaff, AZ 86002-1149; jbenson@nofs.navy.mil, djh@nofs.navy.mil.
[3] Remote Sensing Division, Code 7210, Naval Research Laboratory, 4555 Overlook Avenue, Washington, DC 20375; mozurk@nrl.navy.mil, tom.armstrong@nrl.navy.mil, hindsley@nrl.navy.mil, gilbreath@nrl.navy.mil, rickard@nrl.navy.mil.
[4] Lowell Observatory, 1400 West Mars Hill Road, Flagstaff, AZ 86001; nmw@lowell.edu.

fringes. Long delay lines (LDLs), which use pop-up mirrors to switch in and out additional optical path, are being installed (Clark et al. 1998) and will enable observations on all baselines included in the original design, with maximum baselines of about 435 m in length.

2.2. *Beam Combination and Fringe Detection*

The original three-beam combiner has been expanded into a six-beam combiner simply by adding a mirror, M3B (see Fig. 1), which injects the next three beams at the back of the first beam splitter (BS) to combine with the original three beams. After interferometric combination (BC), three combined beams contain the light from four stations each. (Three complementary output beams from the other side of BC are discarded.) This is the hybrid trait of our beam combiner. An *all-in-one* beam combiner puts all beams onto a single detector. A *pairwise* beam combiner puts single pairs of beams on separate detectors. Our beam combiner is therefore intermediate between these types. (The relative merits of these different designs have been described in Mozurkewich 2000.)

The combined beams, after spatial filtering using pinholes, pass through prism spectrometers and are then collimated onto lenslet arrays and detected by three banks of photon-counting avalanche photodiodes (APDs). The spectral range covered is from 450 to 850 nm. In addition to tracking the fringe motions, each FDL also imposes on its beam a 500 Hz triangle-wave modulation. The resulting delay modulation on a baseline as the difference between two FDL modulations sweeps the fringe pattern of that baseline across the detectors, causing an intensity that varies sinusoidally with time. Changing the amplitude of the modulations (also called *strokes*) changes the frequencies at which the fringes pass over the detectors. Since the three output beams of our hybrid six-beam combiner contain contributions from four input beams, there are six baselines present on each. As long as no two baselines on the same detector have the same fringe frequency, the fringes can be cleanly separated (Mozurkewich 1994). There are many modulation-amplitude solutions that will place the baselines at separate frequencies. The one used for the observations reported here modulated the paths from stations E2, AC, AE, AW, W7, and AN with amplitudes of -1, 4, -3, 3, -4, and 2 (all units in microns), respectively. The presence of multiple baseline separation solutions gives us the freedom to tailor the association of amplitudes to FDLs with respect to the measured FDL responses in order to achieve the best behavior. We have done this, and we typically obtain stroke linearity to better than 1%.

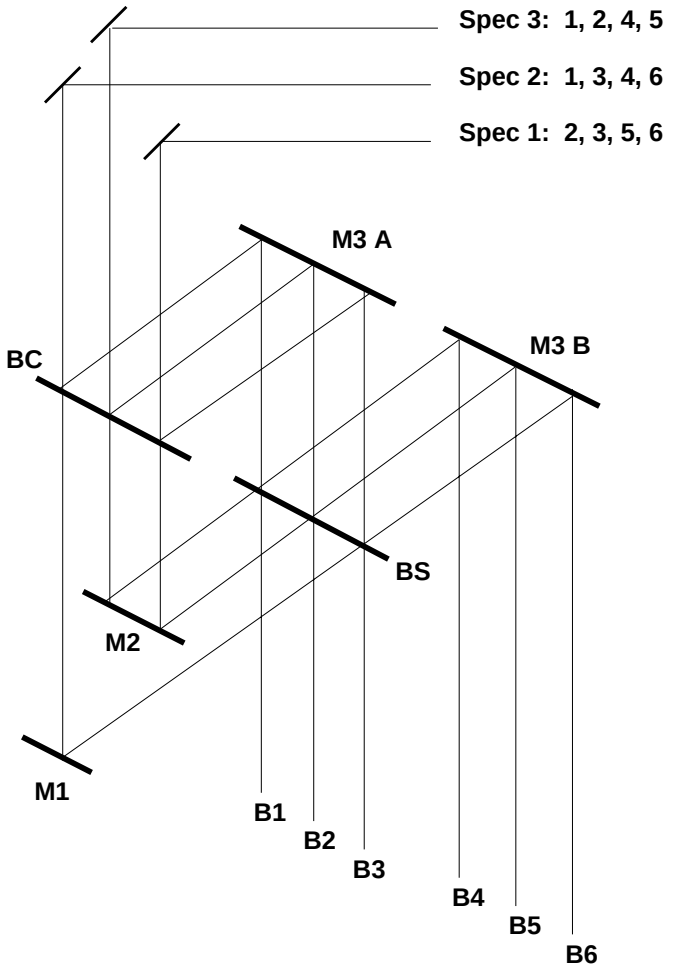

FIG. 1.—NPOI beam combiner. B1 through B6 are the incoming beams, BS and BC are beam splitters. Spectrometers 2 and 3 were used for the reported observations. The three complementary output beams from the other side of BC, which are discarded, are not shown.

2.3. *Fringe Engine Electronics*

Significant upgrades were required in the hardware and software that bin the photons in synchrony with the delay modulation and compute real-time fringe tracking error signals. We have one custom-built triple-height (9U) VMEbus binner board that generates timing signals for 64 bins for up to 32 different wavelength channels. The timing signals are sent over the VMEbus. We have three custom 9U, VMEbus APD processor boards that use the timing signals from the binner board to accumulate the incoming photons into the bins. The APD processor boards have on-board digital signal processors (DSPs) that calculate the real and imaginary components of the Fourier transforms along the bin direction. The DSPs compute the Fourier transforms at eight frequencies. In addition, the real and imaginary components of the Fourier transform along the wavenumber direction at each of the eight frequencies are also computed, to produce the group delay. All computed Fourier values and the bin photon counts are available on the VMEbus.

At present, only the binner board and one of the 32-channel APD processor boards have been integrated into our fringe engine. In order to detect and process six beams with this less-than-complete hardware implementation, we feed the output from two spectrometers to our single APD processor board. Sixteen wavelength channels (570–850 nm) from each spectrometer are fed to separate channels on the 32-channel APD board. This arrangement enables us to observe 11 of the 15 baselines that are available with six stations. One of the 11 baselines appears on both spectrometers. The beam combinations entering any two spectrometers are sufficient to phase the array. We give the baseline layout for the two spectrometers in Table 1.

The 64-bin by 16-wavenumber channel photon counts, called a *fringe frame*, and the Fourier values are read over the VMEbus by a 68060 CPU at a 500 Hz frame rate. The Fourier values along the wavenumber axis, that is, the group delay, are used by the CPU to calculate the fringe

TABLE 1
CURRENT BASELINE LAYOUT

	Spectrometer 2 (OB 1)[a]			Spectrometer 3 (OB 2)[a]		
Bl[b]	Baseline	Modulation (μm)	Proj. Length[c] (m)	Baseline	Modulation (μm)	Proj. Length[c] (m)
1.....	AE-E2	2	15	E2-AC	5	5
2.....	AE-AW	6	30	AW-AC	1	15
3.....	AN-AW	1	28	W7-AW	7	20
4.....	AE-AN	5	34	W7-AC	8	35
5.....	E2-AN	3	19	W7-E2	3	40
6.....	E2-AW	4	20	E2-AW	4	20

[a] Output beam, i.e., the software ID of this spectrometer used in the plot labels.
[b] Baseline ID in this spectrometer used in the plot labels.
[c] Approximate projected baseline lengths for η Vir observations.

tracking error signals. Our implementation of group-delay fringe tracking has been described in Benson, Mozurkewich, & Jefferies (1998). An extension of this method that includes all baselines and frequencies necessary to keep the array phased is used in our current six-station operation mode. We show fringe-frame examples in Figure 2. The temporal bin widths are adjusted electronically to cover the same fringe phase intervals regardless of channel. Thus, in a channel at 500 nm, half of the photons are discarded with a stroke of 1 μm.

2.4. *Array Phasing and Control System*

Our current array-phasing algorithm is very simplistic. A reference FDL station (AW) and the five baselines connecting the reference station to the other five FDL stations are designated as *tracking baselines*. The fringe tracker then looks only at the frequencies of the designated tracking baselines in order to calculate and apply its fringe tracking error signal. The error signal is always applied to the nonreference FDL. The beam-combiner design, the thermal stability of the beam-combining room, and the judicious choice of tracking baselines ensure that once all five tracking baselines are locked on, the array is truly phased up, that is, fringes on all 15 baselines provided by the six beams are present and constrained by the tracking baselines. This simple algorithm is sufficient to keep the array phased and is within the capabilities of our current CPUs. More sophisticated real-time co-phasing fringe tracking algorithms, such as one without a designated reference station but instead using a chain of short baselines connecting any two stations ("bootstrapping"), will enable us to track larger sources. We have purchased the faster CPUs that will support their implementation.

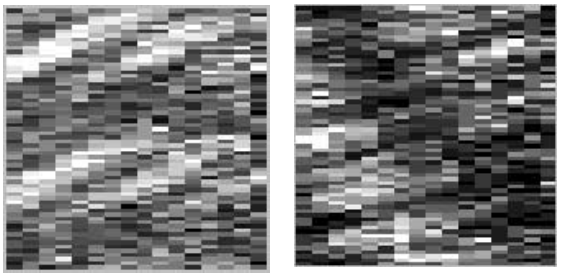

FIG. 2.—NPOI fringe frames for spectrometer 2 (*left*) and spectrometer 3 (*right*). The 16 wavenumber channels are along the *x*-axis; the 64 phase bins are along the *y*-axis. One can clearly see in the figures at least two fringe patterns superposed on each other. The frequency of a fringe along the *x*-axis is a measure of the delay offset on this particular baseline.

The new observer-level control system is based on a graphical user interface that provides various buttons for common actions pertaining to the various subsystems, such as the narrow-angle tracking system, the FDLs, and the fringe tracking system. After system setup and alignment, selection of a target star causes the control system to acquire the star simultaneously with all available stations. Once this is accomplished, fringe search begins on all tracking baselines. The observer can specify a threshold that corresponds to the minimum fringe amplitude signal-to-noise ratio required before the control system switches from the fringe-search mode to the tracking mode. After all required fringes are acquired, a sequence of 2 ms fringe frames is sent to a data recording computer. After data collection, typically for 90 s, and measurement of the count rate on nearby blank sky, we have finished a *star-scan* sequence. After a star-scan sequence, we do an *off-fringe* bias calibration sequence (see § 4.3), in which the FDLs slew to an off-fringe position and record data. We will soon add a *photometric* sequence in which the flux contributions from the individual beams will also be automatically recorded.

3. OBSERVATIONS

The triple star η Virginis (=FK5 460, HR 4689, HIC 60129; $m_V = 3.89$) had been on a list of multiple stellar system targets suitable for NPOI observations (A. Tokovinin 2000, private communication) and was first observed in February of 2002. It consists of a close pair, component A, and a tertiary component, B, some 130 mas away from A. The close pair contains the primary, Aa, and the secondary, Ab. The observations showed that all three components were well separated and located within the interferometric field of view ($\approx$250 mas). More data were obtained in April, May, and June. The approximate projected baseline lengths for the observation of η Vir are listed in Table 1. In addition, some three-station data were found in the NPOI archive from 1997.

Calibrators interleaved with the program stars were β Virginis (FK5 445) for all of the six-station data, and ζ Virginis (FK5 501) for the three-station data. Even though the former has a larger diameter, it is closer to the program

TABLE 2
CALIBRATION STAR DATA

Star	Name	Spectral Type	V Magnitude	Sky Separation (deg)	Adopted Angular Diameter[a] (mas)
HR 4540	β Vir	F9 V	3.61	7	1.43
HR 5107	ζ Vir	A3 V	3.37	18	0.82

[a] Uniform-disk diameter at 800 nm.

star (see Table 2), which is important for calibration. (The companions in the triple system of β Vir are too faint for the NPOI to see.)

Because of the maintenance schedules associated with the initial commissioning of the siderostats, not all stations were available for all observations reported here. Occasionally, the observer would also switch in and out various stations during the night to study the system response to various seeing conditions. This effectively created different subarrays, and the related information was stored with the data. In addition, the observer was able to set the minimum number of tracking baselines (as opposed to the baselines in fringe-search mode) that would trigger the recording of fringe data. As a result of the reference-baseline tracking algorithm as described in the previous section, fringe search could be in progress at various stations while others were tracking, all while data recording was taking place. We list the dates of observation and the number of visibility measurements made (among other information, discussed below) in Table 3.

4. DATA REDUCTION AND BIAS CORRECTIONS

Procedures for the reduction of the visibility data were similar to those described in Hummel et al. (1998). After decoding the complex visibilities from the raw data frames as described below, the data are averaged in 1 s segments. These intermediate data can then be edited, further processed, and averaged over the length of scans using interactive data analysis software. Additional complexity in the process arises from the sources described in the following. Some issues, such as cross talk and photometry, will be addressed only briefly because they have not been studied yet with sufficient detail.

TABLE 3
OBSERVATION AND RESULT LOG

UT Date (1)	Julian Year (2)	N_{vis} (3)	σ_{maj} (mas) (4)	σ_{min} (mas) (5)	φ (deg) (6)	$\rho_{Aa\text{-}Ab}$ (mas) (7)	$\theta_{Aa\text{-}Ab}$ (deg) (8)	$O-C$ (mas) (9)	$\rho_{A\text{-}B}$ (mas) (10)	$\theta_{A\text{-}B}$ (deg) (11)	$O-C$ (mas) (12)
Mar 15	1997.2013	178	0.61	0.13	175.5	5.6	297.6	0.11	141.8	1.6	0.21
Apr 16.....	1997.2890	276	0.62	0.13	174.5	8.9	124.4	0.07	138.9	4.4	0.38
Apr 18.....	1997.2944	340	0.59	0.13	175.4	8.9	128.3	0.13	138.3	4.5	0.03
May 7.....	1997.3465	82	0.65	0.12	176.7	6.3	181.5	0.24	136.9	4.5	0.24
May 8.....	1997.3492	167	0.61	0.12	175.6	6.5	186.0	0.21	137.4	4.5	0.19
Feb 15.....	2002.1240	1262	0.22	0.12	154.3	5.6	317.5	0.06	112.9	151.7	0.22
Feb 23.....	2002.1459	435	0.18	0.17	53.8	4.4	19.4	0.00	113.9	151.6	0.24
Feb 27.....	2002.1569	750	0.19	0.17	171.0	5.0	52.4	0.31	114.7	151.6	0.23
Feb 28.....	2002.1596	2445	1.15	0.05	147.5	5.1	62.5	0.06	114.7	151.6	0.43
May 15.....	2002.3677	1824	0.20	0.18	105.2	6.2	86.9	0.09	118.6	156.3	0.04
May 16.....	2002.3704	800	0.19	0.17	162.0	6.5	91.2	0.10	118.8	156.3	0.02
May 18.....	2002.3759	1136	0.23	0.17	74.4	7.1	98.8	0.13	119.3	156.4	0.10
May 19.....	2002.3786	6320	0.24	0.11	143.3	7.4	102.8	0.08	119.4	156.5	0.02
May 20.....	2002.3814	2624	0.21	0.17	112.1	7.6	106.1	0.10	119.6	156.6	0.04
May 23.....	2002.3896	2528	0.20	0.17	95.4	8.2	115.0	0.12	120.0	156.8	0.03
May 24.....	2002.3923	4608	0.25	0.14	130.7	8.5	117.7	0.04	120.0	156.9	0.11
May 25.....	2002.3950	2912	0.20	0.13	142.2	8.6	119.9	0.09	120.3	157.0	0.08
May 29.....	2002.4060	3232	0.23	0.15	129.2	9.0	131.6	0.32	120.7	157.3	0.04
May 30.....	2002.4087	1472	0.24	0.17	107.3	9.0	130.7	0.17	120.8	157.5	0.09
May 31.....	2002.4115	3360	0.22	0.14	132.6	9.1	134.2	0.01	120.7	157.5	0.11
Jun 2	2002.4170	1936	0.24	0.14	128.9	9.0	138.0	0.11	121.0	157.8	0.07
Jun 3	2002.4197	1312	0.22	0.15	133.3	9.0	140.5	0.05	121.0	157.8	0.07
Jun 4	2002.4224	1776	0.22	0.16	134.1	8.9	143.8	0.11	121.0	158.0	0.03
Jun 5	2002.4252	1120	1.30	0.19	145.4	8.7	145.3	0.07	121.0	158.0	0.09
Jun 6	2002.4279	3504	0.26	0.13	135.0	8.6	147.8	0.05	121.2	158.2	0.17
Jun 7	2002.4306	2480	0.23	0.17	104.6	8.6	150.2	0.03	121.1	158.3	0.05
Jun 8	2002.4334	1824	0.21	0.19	134.9	8.4	153.5	0.08	121.1	158.4	0.08

4.1. *Visibilities*

The four beams present on the spectrometer produce six superposed fringe patterns. The intensity I_{1234} on one of our spectrometer detectors that contains four beams (1234) is given by

$$\begin{aligned} I_{1234}(x,\lambda) &= (\epsilon_1+\epsilon_2+\epsilon_3+\epsilon_4)(\epsilon_1^*+\epsilon_2^*+\epsilon_3^*+\epsilon_4^*) \\ &= \epsilon_1\epsilon_1^*+\epsilon_2\epsilon_2^*+\epsilon_3\epsilon_3^*+\epsilon_4\epsilon_4^*+2\sum_{l\neq m}\epsilon_l\epsilon_m^* \\ &= I_1+I_2+I_3+I_4 \\ &\quad +2\sum_{l\neq m}\sqrt{I_lI_m}|\gamma_{lm}|\cos\left(\frac{2\pi x_{lm}}{\lambda}+\psi_{lm}\right), \end{aligned} \tag{1}$$

where ϵ is the electric field amplitude, $\gamma_{lm}=|\gamma_{lm}|\exp i\psi_{lm}$ represents the complex degree of coherence (visibility) between beams l and m, and x is the FDL delay error including modulation. The expectation value for the photon count rate in a phase bin j integrated over a wavelength channel can be written as

$$b_j=\sum_{i=1}^{4}I_i+\sum_{l\neq m}\frac{\sin(\pi k/n)}{2\pi k/n}\sqrt{I_lI_m}|\gamma_{lm}|\cos\left(\frac{2\pi kj}{n}+\phi_{lm}\right), \tag{2}$$

where k (i.e., k_{lm}) represents the frequency of the fringe for the l-m beam combination and $n=64$ is the number of phase bins. The sinc term is the fringe contrast reduction factor due to the averaging over the finite-width bins. The real and imaginary parts of the visibility are given by the Fourier transform of the bin counts b_j:

$$\begin{aligned} X_k &\equiv \mathrm{Re}\,(V_k)=\sum_{j=0}^{n-1}b_j\cos(2\pi jk/n), \\ Y_k &\equiv \mathrm{Im}\,(V_k)=\sum_{j=0}^{n-1}b_j\sin(2\pi jk/n), \end{aligned} \tag{3}$$

where V_k, the complex visibility on the baseline associated with k, represents our measurement of γ. The unbiased estimator of the squared amplitude of the complex visibility is given by

$$\begin{aligned} V_k^2 &= C_k\frac{\langle X_k^2+Y_k^2-\sum_j\sigma^2(b_j)\rangle}{\left(\langle\sum_j b_j\rangle-B-D\right)^2}, \\ C_k &\equiv \frac{(\alpha_k+1)^2}{4\alpha_k}\left[\frac{2\pi k/n}{\sin(\pi k/n)}\right]^2, \end{aligned} \tag{4}$$

where $\alpha_k=I_l/I_m$, $B=I_i+I_j$ represents the bin counts that are *incoherent* with respect to beams l and m, $\sum_j\sigma^2(b_j)$ represents the bias correction that is due to the variance of the noise process that corrupts the bin counts, and D represents the dark count. The angle brackets denote an average.

In Figures 3 and 4, we plot the average square modulus of the fringe visibility (in channel 1 at 850 nm) as a function of k for a scan on β Vir. [The average in eq. (4) was taken over 500 samples of 2 ms, and the resulting V^2-values were averaged over the length of the scan. For the bias term, $\sum_j\sigma^2(b_j)$, we used $\sum_j b_j$, the total photon count, N, of the frame. No correction due to incoherent flux from other stations and the background were included, i.e., $B=0$, $D=0$, and $\alpha_k=1$.] It can be seen that signals from all six baselines are present in both spectrometers, that is, at $k=1,2,3,4,5$, and 6 in spectrometer 2 and at $k=1,3,4,5,7$, and 8 in spectrometer 3. (The photon rate in spectrometer 3 is lower than that of spectrometer 2 because it has the smaller of the two installed pinhole spatial filters. The additional spatial filtering also causes higher visibility amplitudes in the former.)

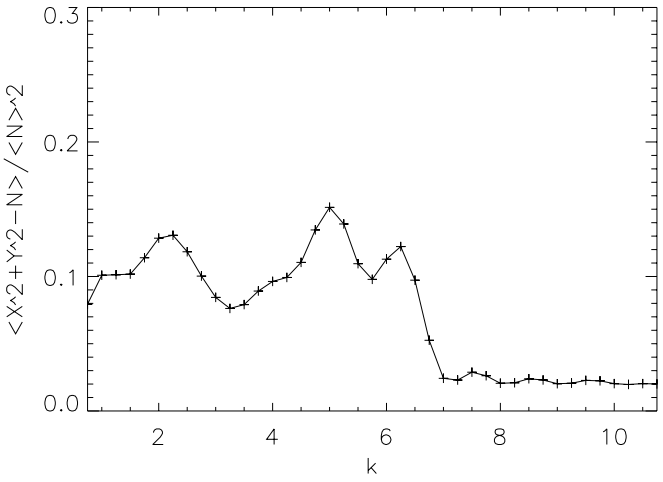

FIG. 3.—Squared visibility amplitude V^2 as a function of fringe frequency k for a scan on β Vir. The average photon rate was 107 per 2 ms in

The reason for the different height of the peaks in Figure 3 and especially in Figure 4 are the different intensities I_i received from the stations. Just before the scan shown, a photometric sequence had been recorded on γ Geminorum some 90° away from β Vir to give the following relative intensities for the stations in spectrometer 3: 0.21 (E2), 0.20 (AC), 0.46 (AW), and 0.13 (W7). Using these numbers with equation (4), the squared visibility amplitude for all six baselines of spectrometer 3 were within 15% of 0.77. This (uncalibrated, squared) visibility amplitude is similar to amplitudes achieved with the three-station system under good seeing conditions.

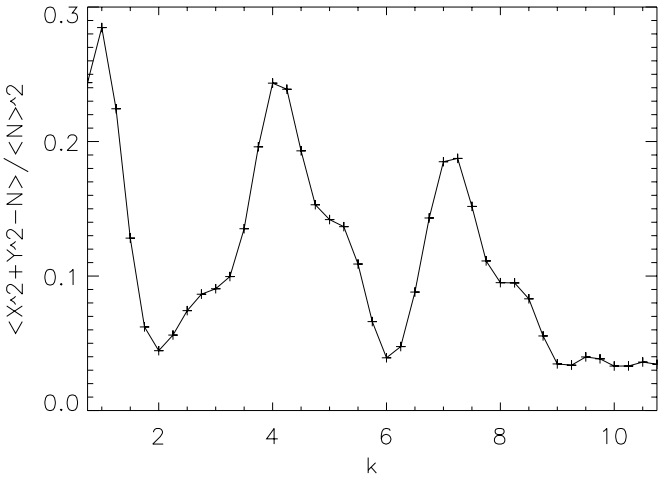

FIG. 4.—Same as Fig. 3, but for channel 1 (850 nm) of spectrometer 3. The average photon rate was 33 per 2 ms.

4.2. *Editing*

The control system did not at the time record which stations (or reference baselines) were in fringe-search mode while data recording was in progress. This is of concern if the observer does not require all stations in the subarray to be tracking a fringe for the data recording to be activated. After study of the delay-line motion in search mode, it was decided to store the 1 s median absolute difference of successive raw (i.e., 2 ms samples) delay measurements as the error of a delay measurement. Search mode is then indicated by median differences that are about a factor of 10 smaller than the differences during actual fringe tracking. As an example, Figure 5 shows small delay variances for the second scan, indicating that the delay line was not tracking the rapid atmospheric fringe motion.

Because of the increased volume of the recorded and decoded fringe data, as well as auxiliary data such as the total tip-tilt detector counts and delay-line positions, we implemented a hierarchical editing scheme in the off-line analysis software that recognizes the interdependencies of the various data types. For example, if a delay value is flagged as bad, so will automatically be all visibility data on baselines involving the particular delay line (i.e., station). This allows one to more efficiently flag bad data by identifying the root causes for it.

4.3. *Bias Correction of Squared Visibility Amplitudes*

For ideal photon-counting detectors, the numerator term $\sum_j \sigma^2(b_j)$ in equation (4), by virtue of the Poisson statistic for photons, reduces to the summed photon counts $\sum_j b_j$. Real photon detectors can depart significantly from ideal detectors by having traits such as read noise, gain, and dead time. These three common non–ideal-detector statistics can be incorporated into the $\sum_j \sigma^2(b_j)$ term by a power-law model of the form

$$\sigma^2(b) = \sigma_0 + \sigma_1 b + \sigma_2 b^2 \ . \tag{5}$$

In this model, an ideal photon detector would have the σ_0 and σ_2 coefficients equal to zero and $\sigma_1 = 1$. This would be the classical Poisson case, in which the detection statistics contribute only an additive bias term ($\sum_j b_j$). Measurements of stellar limb darkening with the photomultiplier tubes of the Mark III interferometer have benefited from such ideal behavior (Quirrenbach et al. 1996). Read noise contributes to σ_0, gain (such as after-pulsing in APDs) contributes to σ_1, and dead time contributes to σ_2. It can be shown that the detection statistics, in the presence of a finite σ_2, introduces a *cross-talk* term in V^2_{lm} that is proportional to the summed V^2 on all of the other baselines that appear on the detector. These cross-talk bias terms can be determined from measurements of V^2 at non–signal fringe frequencies. We show in Figures 6 and 7 fringe power spectra as a function of the fringe frequency k for an off-fringe scan immediately following the scan shown in Figures 3 and 4. Note that the bias level is about the same as the nonsignal level in the coherent scans, indicating that cross talk is not significant here.

Off-fringe measurements can be used to determine the bias terms that do not depend on the fringe visibility (e.g., the σ_0 and σ_1 terms in the model discussed above). Hence, for each on-fringe scan, one should record a corresponding off-fringe scan. Since determining the coefficients of equation (5) from off-fringe measurements would also include the effects of scintillation, we adopted an extension

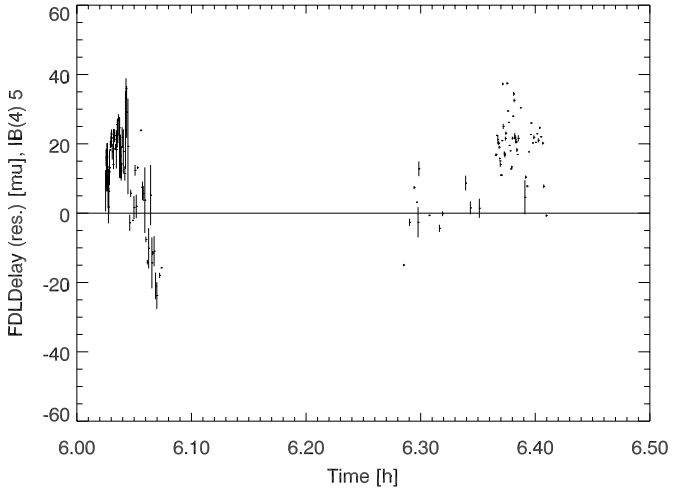

FIG. 5.—The 1 s averages of the residual delay (in microns) of two scans on η Vir on the W-W7 baseline. The error bars are equal to the 1 s median absolute difference between successive delay positions. The fringe was tracked only in the first scan, as indicated by the larger error bars, due to atmospheric fringe motion.

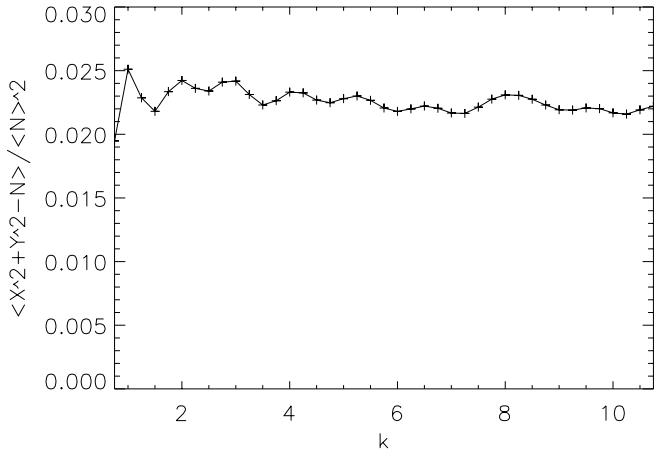

FIG. 6.—Squared visibility amplitude V^2 as a function of fringe frequency k for an off-fringe scan on β Vir (a calibrator) for spectrometer 2.

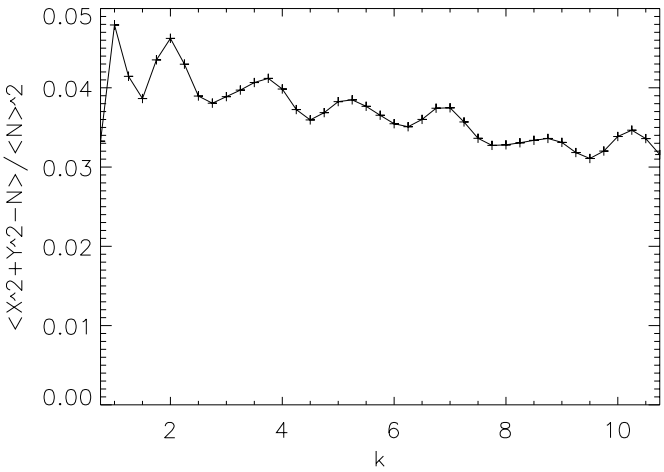

FIG. 7.—Same as Fig. 6, but for spectrometer 3

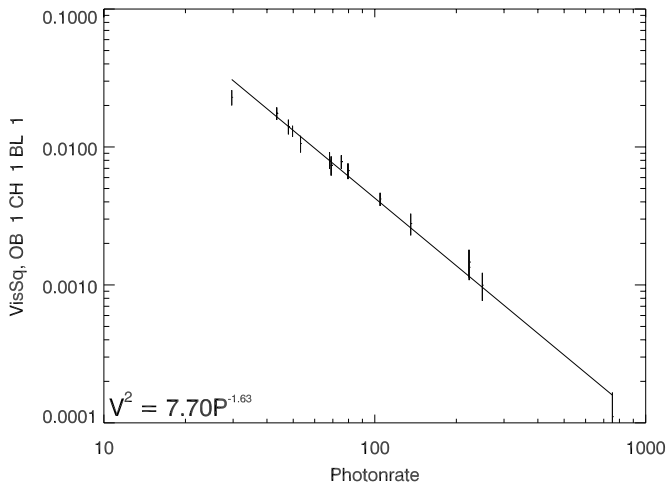

FIG. 8.—Squared visibility amplitude on the E-E2 baseline ($k = 2$) as a function of photon rate for all off-fringe scans with the six-station configuration. Data corresponding to η Vir (FK5 460) and its calibrator (FK5 445) have approximate photon rates of 50 and 100 counts per 2 ms, respectively. Coefficients of a linear fit are given.

of an empirical calibration procedure (Wittkowski et al. 2001) that we used with our three-station data, where there were only two beams on each detector. This procedure is also useful for the observations presented here, since off-fringe scans had not always been recorded for every scan but, rather, once for every star and subarray configuration. Briefly, as a substitute for the bias correction in the case of Poisson noise [$\sum_j \sigma^2(b_j) = N$ in eq. (4)], we used the amplitude at $k = 10$. Then the squared visibility amplitudes of the off-fringe scans are averaged over the length of a scan and plotted versus the photon rate in a log-log diagram (Fig. 8). The linear dependence in such a diagram for the two quantities is modeled by a straight-line fit, and the averaging is repeated using the fit coefficients to predict a bias compensation for the coherent scans. In order to improve the reliability of this procedure, only scans on η Vir and its calibrator have been used to determine the fit coefficients. Also, the bias coefficients were computed for each subarray separately.

4.4. *Bias Correction of Closure Phases*

The complex triple products (i.e., the products of three complex visibilities on baselines forming a triangle), which are vector-averaged, suffer from a bias if two or all three baselines were recorded on the same detector. This is due to correlated noise, and it was shown by Wirnitzer (1985) that the bias can be compensated for by subtracting a bias term, $V_{ijk}^{\rm bias}$, from the real part of the complex triple product. In the case of all three baselines on the same detector, the expression is

$$V_{ijk}^{\rm bias} = (X_{ij}^2 + Y_{ij}^2) + (X_{jk}^2 + Y_{jk}^2) + (X_{ki}^2 + Y_{ki}^2) - 2N_{ijkl} \, . \tag{6}$$

Here X_{ij} and Y_{ij} are the real and imaginary parts, respectively, of the complex visibility on baseline ij (see also eq. [3]) and N is the total number of photons (from all stations) recorded in the frame. This bias is significant and can amount to 10° or more for NPOI data. It is much smaller if only two baselines are recorded on the same detector and the third is from another one, and we have therefore not done bias compensations for this case. (There is no bias if all three baselines are detected on independent detectors, as was the case with the three-station NPOI array.)

5. VISIBILITY CALIBRATION

The calibration of the visibility amplitudes, triple amplitudes, and closure phases follows the same procedures as described in Hummel et al. (1998). Instrumental and seeing-related errors can be measured using the (nearly) unresolved calibrator stars because of the known theoretical response of an interferometer to an unresolved source. The diameter of the calibrator star β Vir, small but nevertheless significant, was estimated from the apparent visual magnitude V and the $R-I$ color index (Mozurkewich et al. 1991). The uncertainty of the diameter is estimated to be 10%. The angular diameter of ζ Vir was taken from Blackwell, Lynas-Gray, & Petford (1991), who used the infrared flux method. The calibrator star data are listed in Table 2. Uncertainty estimates of the calibrated data were based on statistical uncertainties alone. Many of the nights did not have a sufficient number of calibrator observations for an independent and conservative estimate of the calibration uncertainty in each of the subarray configurations used. The model fits, discussed below, indicate that the uncertainties of the squared visibilities were thus underestimated by about a median factor of 2.2. This is in line with results quoted by Wittkowski et al. (2001) for NPOI data. As far as the phase calibration, it is an interesting feature of the hybrid six-station beam combiner used for these observations that closure phases using baselines on the same detector do not actually need calibration, as all internal path lengths are always equal (Mozurkewich 1994). There are a total of 12 triple-baseline combinations for the six stations and two detector arrays we are using, but not all triples are independent, that is, not all can be written as an algebraic sum of other combinations. For the four ($n = 4$) stations in each of the two detector arrays used here, there are three $[(n-1)(n-2)/2]$ independent triple combinations.

While the calibration of the closure phases is straightforward and reliable, the amplitude calibrations have proved to be poorer. We attribute our difficulties in calibrating the amplitudes well to a number of effects that need more study. One possible problem is the insufficient number of bias measurements. The magnitude of the bias is not much less than the uncalibrated visibility amplitudes for η Vir, whereas it is much lower for the calibrator, because it produces photon count rates about twice as high. Another problem could be related to changes in the relative flux levels between stations contributing to the same detector. For the single-baseline case, the denominator in equation (4) simplifies to $\langle \sum_j b_j - D \rangle^2$, where D is the estimate of the dark count. Because the total photon counts ($\sum_j b_j$) are usually much larger than the dark count, the denominator term is not overly sensitive to errors in the estimate of the dark count. But in the case of four beams (i, j, l, m) on the detector, the denominator is $\langle \sum_j b_j - I_i - I_j - D \rangle^2$. Now, in addition to the measured sum of the bin photon counts, one must also obtain estimates of the photon counts contributed by the additional beams that do not contribute to the l-m coherent combination. As the individual beam fluxes are similar, errors in the estimates of the these terms in the denominator are important. The photometric sequence

mentioned in § 2.4 is to be included in future observations. For the observations presented here, we calibrate different subarrays (e.g., E2-AE-AW-AN, or E2-AC-AE-AW, or all six stations) independently to avoid having to normalize the visibilities with the station flux levels.

In dealing with the calibration issues, it was noticed that a single multiplicative factor could be applied to all visibilities on a baseline independent of the channel in order to remove much of the systematic error seen when comparing the data with the model (as discussed below). Even though this procedure introduces more parameters in the model-fitting process, it had been used successfully by Hummel et al. (1995) in the case of the double star Mizar A. There, a tertiary component outside the interferometric field of view but inside the *photometric* field of view was changing the incoherent flux level on the detector in such a way as to change all visibilities on a specific baseline by the same multiplicative factor. The only penalty for using the adjustable baseline calibration factors is the degradation of the photometric information in the data—for example, the ability to measure the precise magnitude differences between binary components and the ability to infer their diameters. If the semiperiodic visibility variation induced by a binary as a function of spatial frequency, which corresponds to variation of the visibility of a single scan with channel index, has more than one period, then the *astrometric* results are much less affected by the floating calibration. We therefore went ahead with this analysis, but we caution that the modeling results presented in the next section are necessarily preliminary. Some visibility amplitude and phase data are shown in Figures 9–12.

6. IMAGING

In an interferometer, each combination of two telescopes, called a baseline, measures the source at a single spatial frequency (coordinates u and v, measured in units of wavelength). Since the number of baselines increases with $n(n-1)/2$, where n is the number of telescopes in the array, the synthesized aperture is sampled more densely as n increases and even more so if Earth rotation is used to change the projection of the baselines onto the sky. Even when missing some spatial frequencies, a unique image can be reconstructed from the data, provided the source is smaller than the inverse of the largest hole in the spatial frequency coverage. With limited data, only sources of limited complexity can be imaged, or a limited number of structural components can be fitted to the data.

For the purpose of the present analysis of the triple star η Vir, we use imaging techniques to provide initial estimates of the component positions for the modeling algorithm to be discussed in the next section. We used the AIPS software package developed by NRAO for interferometric imaging of radio data. We converted our data into complex baseline-based visibilities by taking the square root of the squared amplitudes, and by solving for a set of baseline phases meeting the requirement that the measured triple combinations yield the same closure phases. The latter was done by using a singular-value decomposition method to handle the degeneracy in the system of linear equations caused by the fact that the number of independent closure phases is less than the number of baseline phases. [The ratio of these numbers is $(n-2)/n$, where n is the number of stations.] We used standard phase self-calibration methods and the

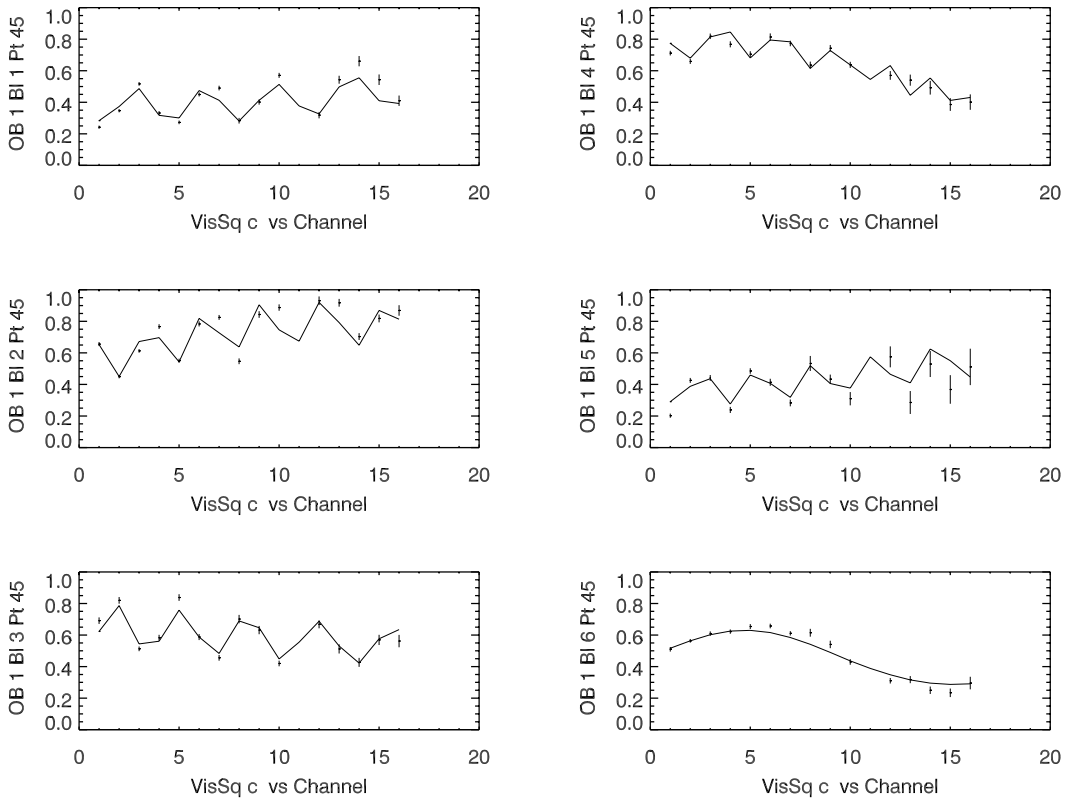

FIG. 9.—Squared visibility data and model for the six baselines of spectrometer 2 on 2002 February 15

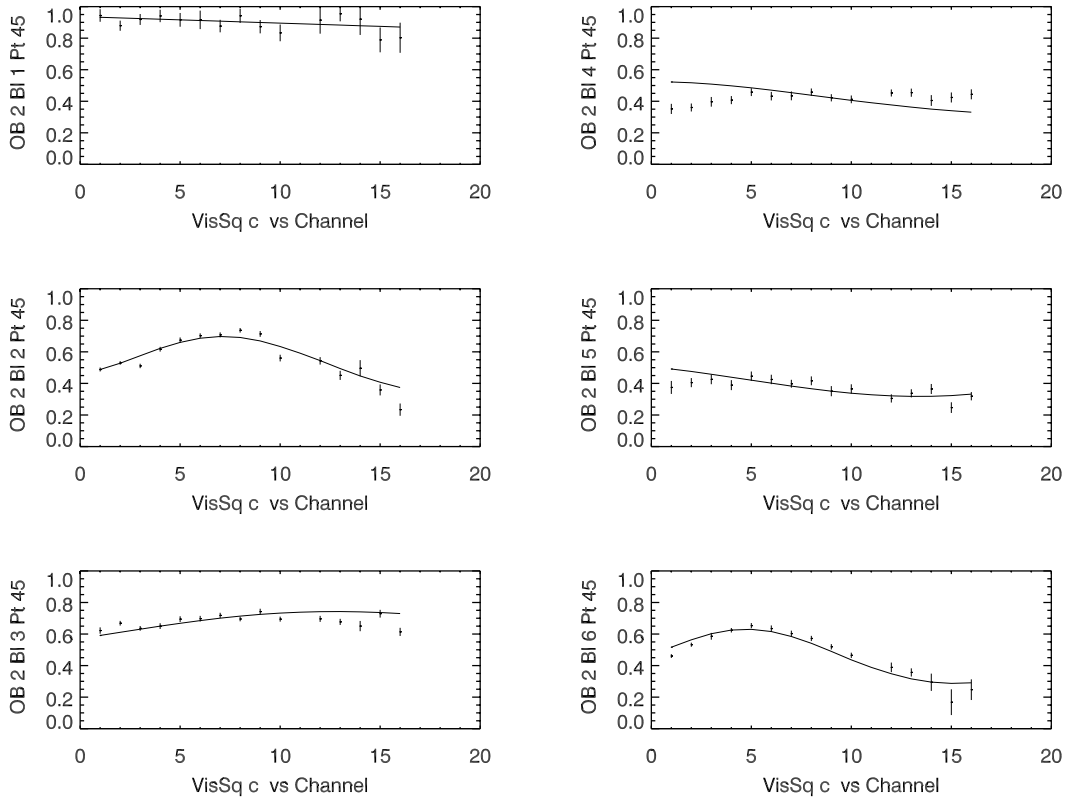

FIG. 10.—Same as Fig. 9, but for spectrometer 3

CLEAN algorithm to deconvolve the Fourier transform of the visibility data from the sidelobes of the synthesized point-spread function, arriving at the images shown in Figures 13 and 14. One can clearly see the orbital motion both of the close pair and of the wide pair. In Figure 15, we show the coverage of the *uv*-plane provided by the 13 scans taken on May 19.

We combined the data of all channels for the images we presented, as the spectral types of all three components are sufficiently close to each other. If this were not the case, the source structure would depend on wavelength and the data of each channel would have to be imaged separately. However, because much fewer data are available for individual channels, the resulting point-spread functions would suffer from significant sidelobes, making the CLEAN deconvolution difficult. One solution to this problem might be found by combining the imaging algorithm with adjustments of parameters describing the wavelength dependence of the source structure. For stellar observations, a suitable parameter would be the effective temperature, assigned to individual CLEAN components during the deconvolution. The

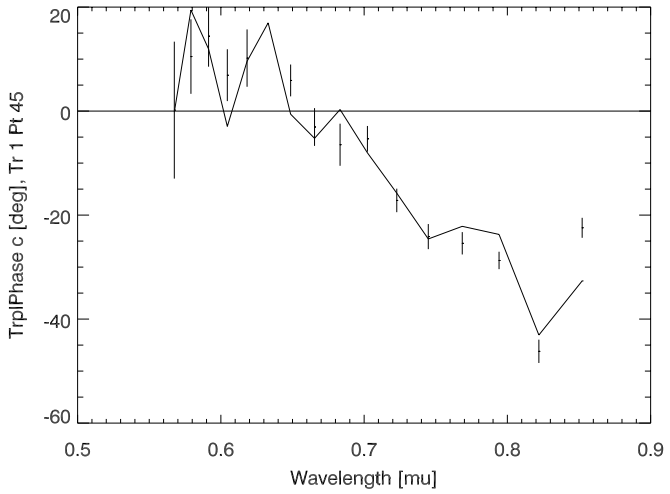

FIG. 11.—Closure phases (in degrees) and model for the triple (E2-AE) − (AW-AE) + (AW-E2), all baselines on spectrometer 2, on 2002 February 15.

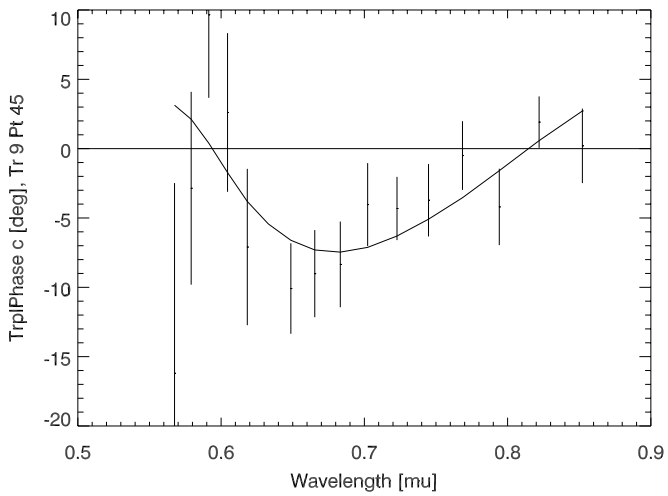

FIG. 12.—Closure phase data and model for the triple (AC-E2) − (AC-AW) + (AW-E2), all baselines on spectrometer 3, on 2002 February 15.

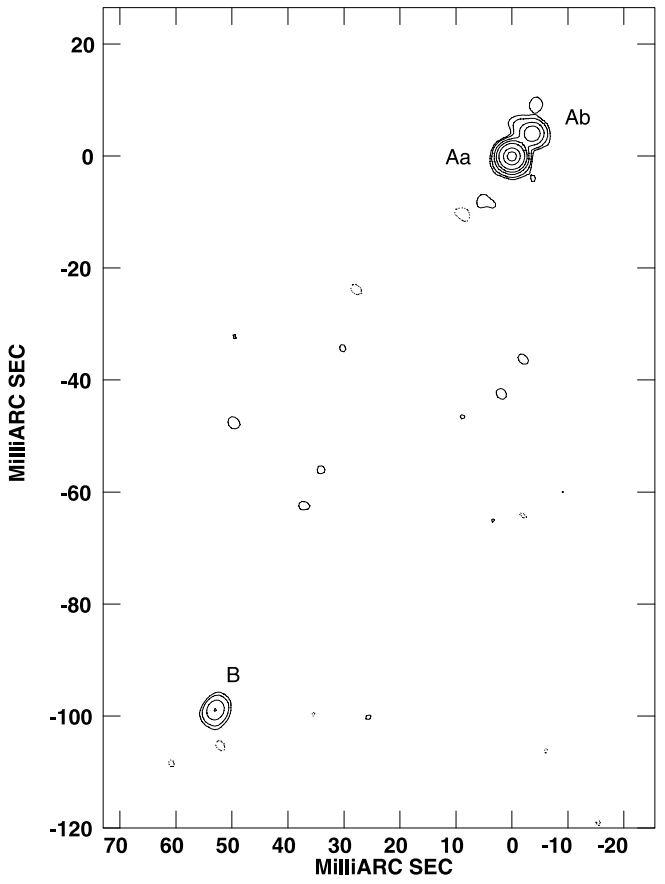

FIG. 13.—Image of η Vir on 2002 February 15. Contour levels are -1%, 1%, 2%, 5%, 10%, 20%, 50%, and 80% of the peak. The map was restored with a circular Gaussian of 3 mas diameter.

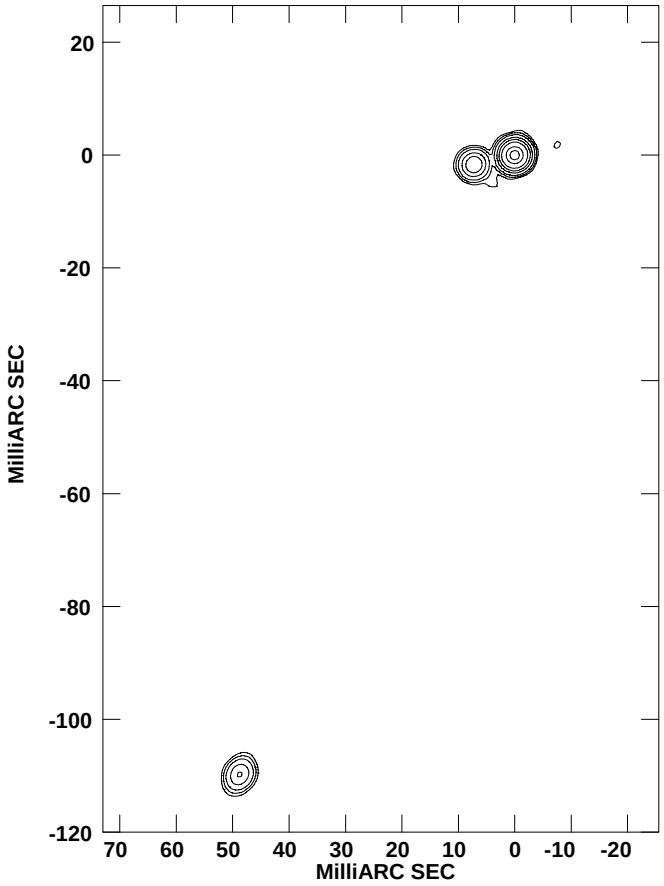

FIG. 14.—Image of η Vir on 2002 May 19. Contour levels are -0.5%, 0.5%, 1%, 2%, 5%, 10%, 20%, 50%, and 80% of the peak. The map was restored with a circular Gaussian of 3 mas diameter.

computation of the model visibilities for the purpose of phase self-calibration could then take the effective temperatures into account. This algorithm would be iterated with adjustment of the effective temperature in predefined "isothermal" regions in the map. The broad bandwidth of an interferometer such as the NPOI could then make up for the limited number of elements and still derive high-fidelity maps of stellar surfaces or composite-spectrum binaries.

7. MODELING

7.1. *Preliminaries*

The case we have before us, a triple star system with both pairs resolved, presents the possibility of measuring the mass ratio of the stars in the close pair by referencing their motion to the tertiary component. Adding the system's parallax to the data would then yield individual masses without the need to obtain radial velocity curves from spectroscopy. A measurement of the trigonometric parallax ($\pi_{\rm trig} = 13.1 \pm 0.8$ mas) is indeed available for η Vir from the *Hipparcos* Catalogue (ESA 1997). However, the close pair is in fact a double-lined spectroscopic binary (No. 718 in the catalog by Batten, Fletcher, & MacCarthy [1989]), and improved orbital elements from spectroscopy, as well as the elements of the long-period binary from speckle interferometry, have been published most recently by Hartkopf et al. (1992, hereafter HK92). All these data taken together provide several ways of assessing their mutual consistency,

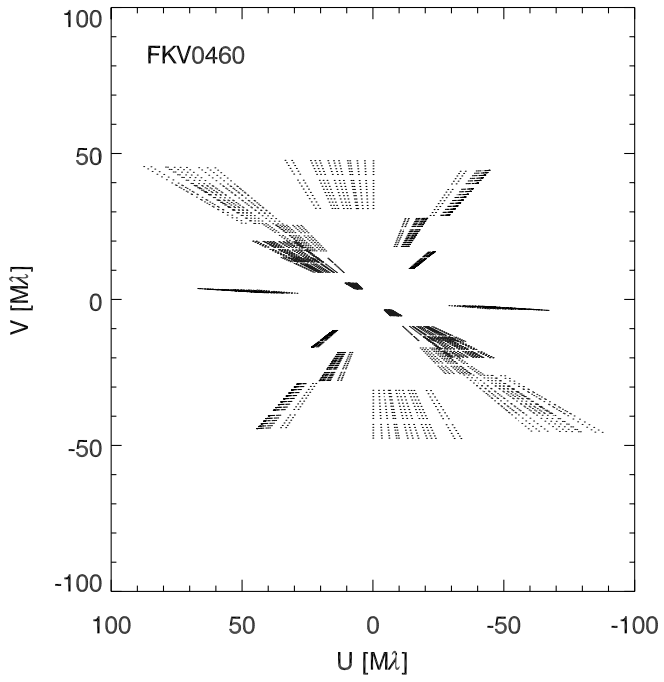

FIG. 15.—The *uv*-coverage of the observation on 2002 May 19. Each radial line corresponds to the measurements in 16 channels for a single scan on a particular baseline.

TABLE 4
ORBITAL ELEMENTS AND COMPONENT PARAMETERS

Quantity	Aa	Ab	B
a (mas)	...	7.36 ± 0.08	133.7 ± 0.1
i (deg)	...	45.5 ± 0.9	50.6 ± 0.2
Ω (deg) (J2000.0)	...	129.5 ± 0.9	170.8 ± 0.2
T (JD − 2,440,000)	...	$12{,}321.4 \pm 0.3$	$7{,}896.2 \pm 0.7$
e	...	0.244 ± 0.007	0.087 ± 0.002
ω (deg)	...	196.9 ± 1.8	2.3 ± 0.4
P (days)	...	71.7916 ± 0.0006	4774.0 ± 4.6
$\mathscr{M}$ ($M_\odot$)	2.68 ± 0.15	2.04 ± 0.10	1.66 ± 0.16
ϕ[a] (mas)	0.46	0.21	0.15
m_V[b] (mag)	4.2	6.0	6.5
γ (km s^{-1})		4.9 ± 0.2	
$\pi_{\rm orb}$[c] (mas)		13.0 ± 0.5	

[a] Adopted from photometry.
[b] From magnitude differences, using $m_{\rm AB} = 3.89$.
[c] Derived.

as well as the derivation of many of the physical component parameters.

In order to model the available data, we developed a hierarchical stellar systems model format. With it, the motions of the stellar components in a multiple system can be separated into binary components, each of which describes, using the seven orbital elements, the motion of its two, possibly multiple, subcomponents around a common center of mass. Such a description is possible if the separation between binary components is much larger than the separation of the subcomponents. Hierarchical systems are the most common type of multiple stellar system, because they are dynamically stable. Our model format also includes parameters of the individual components, that is, their diameters, masses, and brightness magnitudes. The parameters were selected to be as close as possible to actual physical component parameters, such as the masses, but also to be convenient for most types of data, such as those provided by spectroscopy and astrometry. Finally, no parameter must be a combination of other parameters. All parameters ultimately fitted to the combined data as described in § 7.3 are listed in Table 4.

Since we were planning to combine the data we have at our disposal in order to optimally constrain the parameters in the hierarchical model, it was necessary to address an issue related to the overwhelmingly large amount of visibility data (see col. [3] in Table 3). It has been shown in Hummel et al. (1995) that for short-period systems, one must fit the orbital elements directly to the visibility data to account for the orbital motion during the observations. On the other hand, this kind of fit can take an extraordinary amount of computing time for interferometric data sets of the size we have here and for the number of parameters in a model for a triple system. Fortunately, the orbital period of the close pair in η Vir is about 72 days, so the orbital motion effect is small and can be included in a fit of the relative astrometric positions in a binary component (separation ρ and position angle ϕ) to each night of interferometric data. (As a reference epoch, we chose local midnight at the NPOI site, which is UT + 7 hr.) The hierarchical model was then fitted to the combination of radial velocities and astrometric positions derived from both speckle and long-baseline interferometry.

For the model-fitting results we are about to present, it is important to understand the subtle difference between the center of mass and the photometric center. The orbital elements listed in the hierarchical model for a binary component are for the motion of the center of mass of one subcomponent around the center of mass of the other subcomponent, for example, subcomponents Aab (≡A) and B in Aab-B. For the interferometric visibility data, which split all three components, actual stellar component positions for a particular night can be directly derived from the hierarchical model. However, when combining the astrometric data derived from the interferometry with the speckle data, which do *not* resolve the close pair (Aa-Ab), it is necessary to transform the (ρ, θ)-values to describe the relative positions of the photometric centers. This is done by using the stellar masses and brightnesses, which are also part of the hierarchical model.

7.2. *Astrometric Orbits*

We measured component positions in a number of images obtained from interferometry and used these to derive initial estimates for the orbital elements of the close pair. Elements for the wide pair had been published by HK92. Initial estimates for the magnitude differences between the components were then derived by fitting to the interferometric visibility data, using instantaneous positions as predicted by the orbital elements. In this step (and all following iterations), we allowed the baseline calibration factors to float (as described in § 5). The color of the stellar components appeared to be the same across our spectral coverage, which is why we fitted only two magnitude differences ($m_{\rm Ab} - m_{\rm Aa}$ and $m_{\rm B} - m_{\rm Aa}$). However, there was a slight tendency of B to be redder than A by about 0.2 mag at 850 nm compared with 550 nm, but a fit of this number was not considered reliable given the calibration quality. The combined magnitude was adjusted to match the cataloged magnitude for η Vir ($m_V = 3.89$). The angular component diameters appear to be small, so we did not fit them, especially since the results would not be very reliable, because of our floating baseline calibration constants. Rather, we derived predicted uniform-disk angular diameters ϕ from the R–I color indexes (assumed to be identical for all components in η Vir

because of the similar spectral types) and the apparent visual magnitudes, using the calibration derived by Mozurkewich et al. (1991).

In a second iteration, we derived improved positions from fitting to the visibility data of individual nights (with the magnitudes fixed) and then updated the orbital elements. This process was repeated one more time to check the convergence. From this analysis, we derived a mass ratio for the components in the close pair of $\mathscr{M}_{\rm Aa}/\mathscr{M}_{\rm Ab} = 1.27 \pm 0.09$. This is in good agreement with the mass ratio determined from spectroscopy by HK92, $K_{\rm Ab}/K_{\rm Aa} = 1.33 \pm 0.02$, where K is the velocity semiamplitude.

The astrometric single-night fit results are listed in Table 3, where columns (4) and (5) give the semiaxes, and column (6) the position angle of the astrometric uncertainty ellipse; columns (7) through (12) give, for each binary component, the derived separation and position angle (equinox = mean epoch at local midnight on the date of the observation) and the deviation of the fitted relative binary position (ρ, θ) from the combined model prediction (see below). Position angles are measured east from north (counterclockwise). The astrometric uncertainty ellipses are one-seventh the size of a Gaussian fitted to the center of the synthesized point-spread function. The scaling factor was chosen to match the mean of the $O-C$ (observed minus calculated) values. Because of the uncertainty in the amplitude calibration of the visibilities, we chose not to derive the astrometric errors from an analysis of the increase of the reduced χ^2 when varying the position. This would have resulted in very different weights because of the very different number of visibilities measured in each night. Similarly, the uncertainty ellipses for the speckle positions shown in Figure 17 were scaled to provide a reduced χ^2 of unity for the orbital fit because HK92 only specified the relative weights assigned to the speckle data. The relative orbits are shown in Figures 16–19. In these plots, we also show the combined model predictions in the form of connecting lines between the measurements and the predicted position on the orbit (thus their lengths are the $O-C$ values given by cols. [9] and [12] of Table 3). Note that an error in the mass ratio of components Aa and Ab would manifest itself as a poor fit of the model to the measured positions of B, as shown in Figures 18 and 19. This is because the photocenter orbit of A around its center of mass would then have the wrong size, leading to a different size of the model loops.

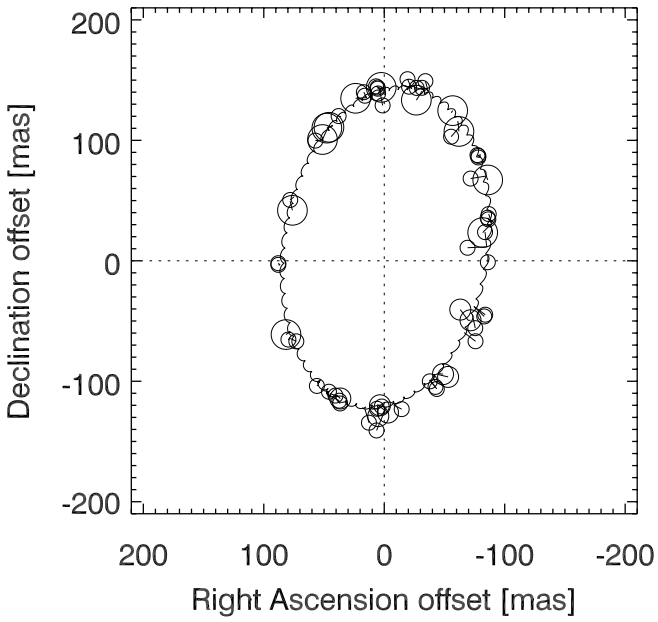

FIG. 17.—Relative orbit of the wide pair, A-B, where A is the photocenter of Aa-Ab. The data shown, all speckle observations, are from HK92. The model loops are due to the motion of the photocenter of A around its center of mass.

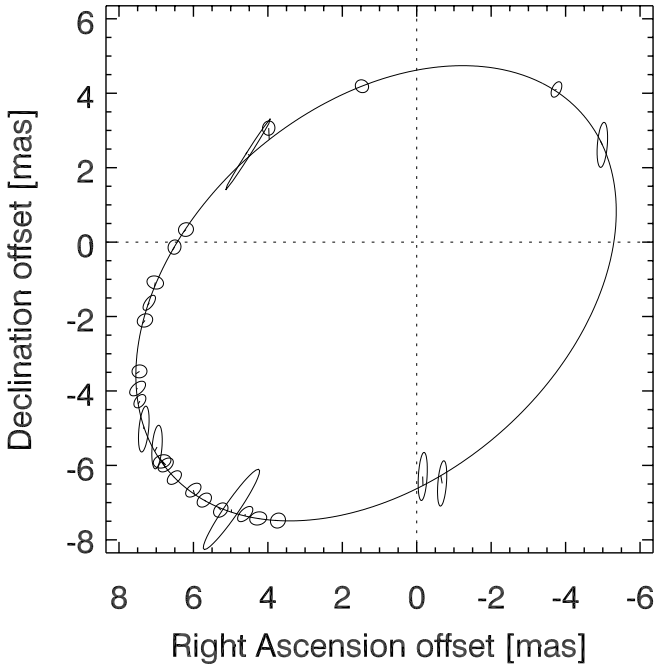

FIG. 16.—Relative orbit of the close pair, Ab-Aa, from NPOI measurements.

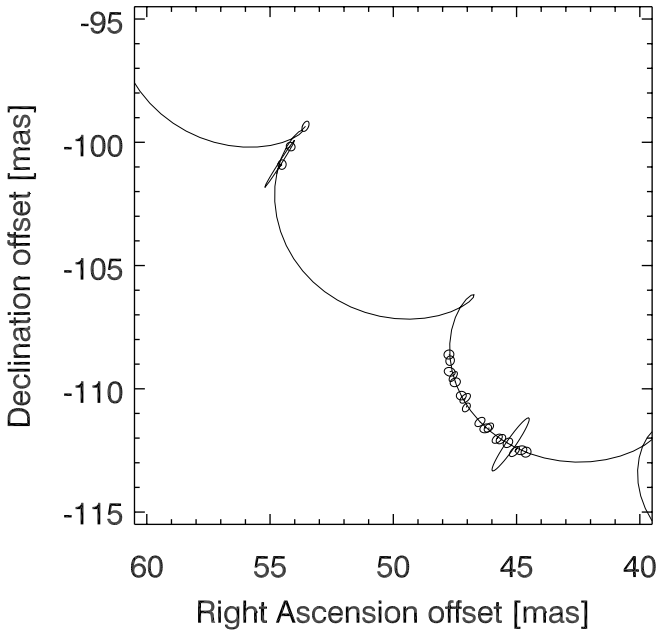

FIG. 18.—NPOI positions for the B component relative to the photocenter of A (lower left quadrant of Fig. 17), with the model orbit for the same time period.

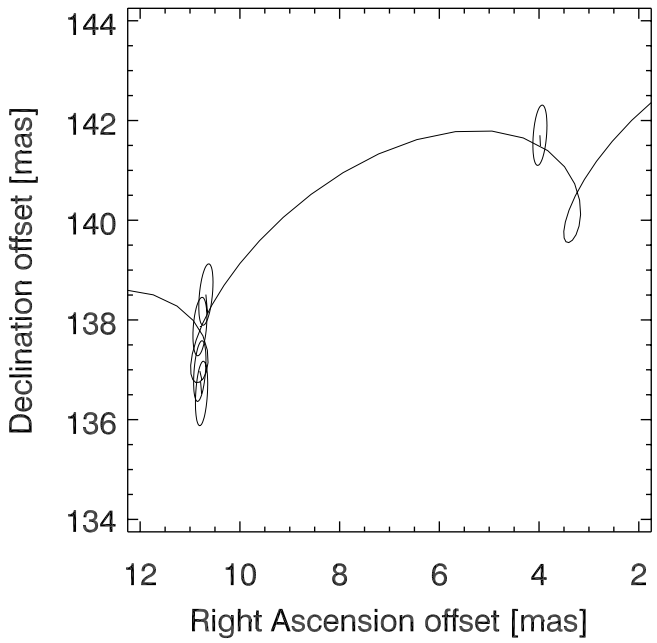

FIG. 19.—NPOI positions for the B component relative to the photocenter of A (upper left quadrant of Fig. 17).

7.3. *Combined Modeling*

The astrometric mass ratio and also the orbital elements derived in the previous section are not significantly different from matching spectroscopic parameters published by HK92 (which is why we do not list these elements again here). Therefore, we combined the astrometric and radial velocity data (taken from HK92 and with uncertainties assigned to normalize the reduced χ^2 of the orbital fit) and adjusted the appropriate hierarchical model parameters slightly for a best fit. The precision of the orbital periods benefits greatly from this combination, because the oldest radial velocity data date back almost a hundred years. In addition, all three individual component masses are now constrained, even though there is no measured radial velocity curve for component B. This is because the double-lined close pair constrains the orbital parallax, which in turn constrains the total mass of the system. Component B then is effectively the unmeasured component in a single-lined binary with astrometric orbit and parallax, which allows one to compute its mass. The combined elements are listed in Table 4, including γ, the systemic velocity of η Vir. The orbital elements of a binary are the semimajor axis a, the orbital inclination i, the angle of the line of nodes Ω (precessed to epoch 2000.0 and measured east from north), the epoch T of passage through the ascending node, orbital eccentricity e, the angle of the periastron ω, and finally the orbital period P. The combined model predictions and the radial velocity data are shown in Figures 20 and 21.

8. DISCUSSION OF ASTROPHYSICAL RESULTS

With respect to the orbital elements and masses, we find general agreement with the results of HK92, except that our mass for the primary component (Aa) is about 15% larger. From the orbital period, semimajor axis, and component masses of the close pair, we compute an orbital parallax of

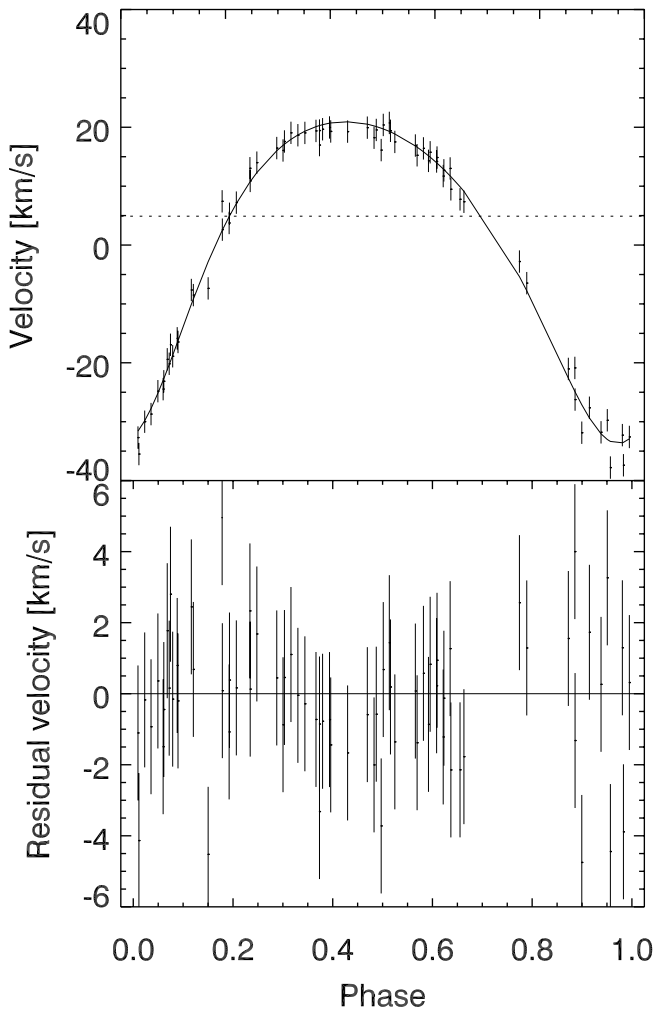

FIG. 20.—Radial velocities from HK92 and our combined fit residuals for component Aa.

$\pi_{\rm orb} = 13.0 \pm 0.5$ mas, which is very close to the trigonometric parallax determined by *Hipparcos* (ESA 1997), $\pi_{\rm trig} = 13.1 \pm 0.8$ mas. The analysis of the *Hipparcos* data for η Vir has been improved by Söderhjelm (1999), who also published orbital elements for the wide pair that are consistent with our results. More importantly, Söderhjelm determined a magnitude difference between components A (Aab) and B of $\Delta H_p = 2.2$ mag, which is much more in line with our result ($\Delta m_V = 2.5$ mag) than what was estimated by HK92. This resolves an inconsistency pointed out by HK92 as to B being less massive but brighter than Ab. Confirmation of the relative magnitudes in η Vir comes from Froeschlé & Meyer (1988), who used the lunar occultation technique to detect all three components. The measured projected angular separation of the wide pair is consistent with the prediction using the lunar motion vector quoted for these observations by Meyer et al. (1995). The projected angular separation of the close pair was measured to be 7 ± 2 mas, compared with our prediction of 4.3 mas. Froeschlé & Meyer (1988) measured magnitude differences of $\Delta m_{\rm Aa\text{-}Ab} = 1.8 \pm 0.2$ and $\Delta m_{\rm Aa\text{-}B} = 2.1 \pm 0.2$ at a wavelength of 410 nm.

The spectral types of Aa and Ab are listed by HK92 as A2 IV and A4 V, respectively. Considering the main-sequence

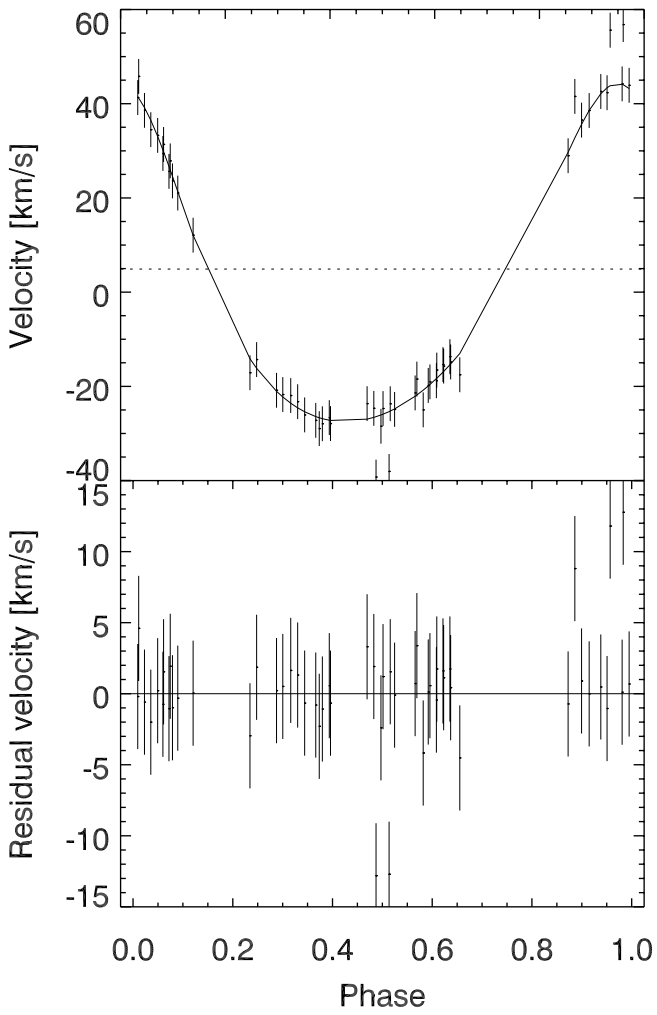

FIG. 21.—Same as Fig. 20, but for component Ab

component Ab first and applying the distance modulus ($D_{\rm mod} = 4.4$), we obtain an absolute visual magnitude $M_V = 1.6$, consistent with its spectral type (Schmidt-Kaler 1982). The same is true for its mass, for which one would expect about 2.1 $M_\odot$ (Andersen 1991). For the luminosity class of the primary component Aa, namely, subgiant, less reliable predictions are available, and we therefore quote the following ranges for a component of spectral type A2 between classes V and III: mass 2.3–2.8 $M_\odot$, $M_V = 1.3$–0.3 mag. From these numbers it can be concluded that the mass and luminosity of component Aa are consistent with its having evolved to a giant of type A2. Component B is the least well known; its spectral type is unknown, as none of its lines have been detected by HK92. This is not surprising, given its magnitude difference to component A. Given the fact that component Ab is still on the main sequence and B is fainter than Ab, component B is likely to be unevolved. A star of type A8 or F0 would be a reasonable match to the measured mass and absolute magnitude, and its color would only be about 0.3 mag redder than the other early type A components. This seems to be consistent with our data, although, as mentioned in § 7.2, a reliable fit of the relative color could not be performed. Well-calibrated visibility data are especially needed for the determination of these color differences.

The answer to the question of coplanarity, which eluded HK92, can now be answered with "no" using the following equation for the relative inclination ϕ between the two orbital planes:

$$\cos\phi = \cos i_1 \cos i_2 + \sin i_1 \sin i_2 \cos\Delta\Omega \qquad (7)$$

(see Fekel 1981). Here i_1 and i_2 are the inclinations of the two orbits and $\Delta\Omega$ is the difference between the two ascending-node angles. For the two orbital planes in η Vir, we get $\phi = 30\overset{\circ}{.}8$, and the two components are co-rotating. According to Fekel (1981), orbital non-coplanarity is not uncommon in close multiple systems. Based on a catalog of multiple stellar systems maintained by himself, Tokovinin (1993) found correlations between the orbital angular momentum vectors in hierarchical triple systems. These correlations have been modeled based on current star formation theories by Sterzik & Tokovinin (2002). From that paper we also learn that there are only 22 systems currently with both orbits measured, and only three with unambiguous determinations of the ascending nodes. Therefore, resolution with interferometry of the close pairs in triple stars could significantly increase the number of well-known systems.

9. CONCLUSIONS

Interferometric imaging benefits most dramatically from the increased amount of data that comes with a larger number of telescopes. This is because the imaging process makes the least number of assumptions about the source structure, whereas the modeling process just needs to have a limited number of predefined structural components, which are then fitted to the data by adjusting their parameters. In this case, even though a triple star is more complex than a double star (assuming unresolved stellar disks), the example does not really do justice to the actual improvement in imaging capability provided by the six stations of the NPOI. However, it is now possible to make an image of a simple double or triple star with as few as just one or two scans, and to measure the stellar positions in order to use these in a model fit of orbital parameters. With more scans and a good calibration, images of stellar surfaces, interacting binaries, etc., would be ideal imaging targets.

We thank B. O'Neill, W. Wack, and S. Nichols for making the observations, as well as NPOI team members for their support of this project. The work done with the NPOI was performed through a collaboration between the Naval Research Lab and the US Naval Observatory, in association with Lowell Observatory, and was funded by the Office of Naval Research and the Oceanographer of the Navy. This research has made use of the SIMBAD literature database, operated at CDS, Strasbourg, France.

REFERENCES

Andersen, J. 1991, A&A Rev., 3, 91
Armstrong, J. T., et al. 1998, ApJ, 496, 550
Batten, A. H., Fletcher, J. M., & MacCarthy, D. G. 1989, Publ. Dominion Astrophys. Obs. Victoria, 17, 1
Benson, J. A., Mozurkewich, D., & Jefferies, S. M. 1998, Proc. SPIE, 3350, 493
Blackwell, D. E., Lynas-Gray, A. E., & Petford, A. D. 1991, A&A, 245, 567
Clark, J. H., Ha, L., Mozurkewich, D., & Armstrong, J. T. 1998, Proc. SPIE, 3350, 497
ESA. 1997, The Hipparcos and Tycho Catalogues (SP-1200) (Noordwijk: ESA)
Fekel, F. C., Jr. 1981, ApJ, 246, 879
Froeschlé, M., & Meyer, C. 1988, Ap&SS, 142, 203
Hartkopf, W. I., McAlister, H. A., Yang, X., & Fekel, F. C. 1992, AJ, 103, 1976 (HK92)
Hummel, C. A., Armstrong, J. T., Buscher, D. F., Mozurkewich, D., Quirrenbach, A., & Vivekanand, M. 1995, AJ, 110, 376
Hummel, C. A., Mozurkewich, D., Armstrong, J. T., Hajian, A. R., Elias, N. M., II, & Hutter, D. J. 1998, AJ, 116, 2536
Hutter, D. J., & Elias, N. M., II. 2002, Proc. SPIE, 4838, 1234
Meyer, C., Rabbia, Y., Froeschlé, M., Helmer, G., & Amieux, G. 1995, A&AS, 110, 107
Mozurkewich, D. 1994, Proc. SPIE, 2200, 76
———. 2000, in Principles of Long Baseline Stellar Interferometry, ed. P. R. Lawson (Pasadena: JPL), 231
Mozurkewich, D., et al. 1991, AJ, 101, 2207
Quirrenbach, A., Mozurkewich, D., Buscher, D. F., Hummel, C. A., & Armstrong, J. T. 1996, A&A, 312, 160
Schmidt-Kaler, T. H. 1982, in Landolt-Börnstein New Series, Group 6, Vol. 2b, Stars and Star Clusters, ed. K. Schaifers & H.-H. Voigt (New York: Springer), 1
Söderhjelm, S. 1999, A&A, 341, 121
Sterzik, M. F., & Tokovinin, A. A. 2002, A&A, 384, 1030
Tokovinin, A. A. 1993, AZh Pisma, 19, 944 (English transl. Astron. Lett., 19, 383)
Wirnitzer, B. 1985, J. Opt. Soc. Am. A, 2, 14
Wittkowski, M., Hummel, C. A., Johnston, K. J., Mozurkewich, D., Hajian A. R., & White, N. M. 2001, A&A, 377, 981